



Establishing a Cold Spray Particle Deposition Window on Polymer Substrate

Jung-Ting Tsai¹ · Semih Akin² · Fengfeng Zhou² · David F. Bahr¹ · Martin Byung-Guk Jun²

Submitted: 21 September 2020 / in revised form: 8 January 2021 / Accepted: 8 February 2021 / Published online: 18 March 2021
© ASM International 2021

Abstract A set of processing conditions for cold spray deposition of an embedded particle layer on a polymer substrate has been established using a dynamic impact model and verified experimentally. This research utilizes a three-network polymer model based on high strain-rate impact tests to capture the nonlinear and time-dependent response of polymer deformation during the cold spray impact with both rigid and deformable particles. The particle's material properties, particle velocity, and particle size were systematically studied to obtain the polymer deformation's various responses from finite element analysis. Particle impact velocity was experimentally measured with a double disk rotary system. The numerical results were mapped into diagrams and validated with the experimental results of cold spraying Cu and Al₂O₃ powders. This research contributes to quantifying the deposition window, which embeds but still exposes metallic/ceramic powders on a polymer substrate.

Keywords cold spray · deposition window · FEA · particle · polymer · three-network polymer model

Introduction

Cold spraying metal or ceramic particles on polymer substrates may increase the anti-abrasive, anti-bacterial, and anti-corrosion of the polymer substrate. Cold-sprayed particles do not require pre-heating, and thus, benefit from any powder coating without the involvement of oxidation. The cold spray technique provides easy maneuverability of the sprayed pattern, a large coating area of surface, and no high spraying temperature requirement. These advantages benefit industrial efficiency and provide an affordable, robust, and rapid method for coating applications (Ref 1, 2).

Prior studies (Ref 3) have reported that the primary method of providing adhesion of a cold-sprayed coating onto a polymer substrate uses mechanical interlocks of the metal/ceramic particles onto the substrate. Particles within the substrate generally preserved their original shape. Cold spraying of copper (Cu) particles onto substrates such as polyurethane, high-density polyethylene, polypropylene, polyamide 6, polytetrafluoroethylene, and polycarbonate showed a general trend that increasing spray pressure allowed deeper penetration, which could be enacted by increasing the propelling gas pressure. However, particle penetration and subsequent layer deposition were influenced by the polymer jetting around the embedded Cu particle. Jetting caused the material to cover the Cu particle and further continue on the polymer substrate's metallization. The plastic deformation of the polymer has a significant impact on the penetration depth. A previous study (Ref 4) has modeled the metal particle impacting a polymer substrate in cold spray coating using the Johnson–Cook plasticity model in the finite element analysis (FEA). The complexities of the deformation behavior of metals and polymer high strain rates make the prediction of particle embedding and substrate deformation challenging and

✉ Martin Byung-Guk Jun
mbgjun@purdue.edu

¹ School of Materials Engineering, Purdue University, West Lafayette, IN 47907, USA

² School of Mechanical Engineering, Purdue University, West Lafayette, IN 47907, USA

often results in developing a process parameter window for cold spraying onto the polymer substrate via a trial error process.

The mechanical response of many polymers at high strain rates is available in literature (Ref 5-12). Typically testing equipment such as Hopkinson bar, Taylor Impact, and Transverse Impact is used to conduct polymer deformation strain rates to validate the polymer model. Some studies (Ref 13) also incorporate polymer impact testing at a low strain rate with temperature consideration. Models for describing large strain polymer network deformation include the eight-chain model, the full network, and the cross-link–slip-link model (Ref 14). A thorough derivation, verification, and validation have been done (Ref 15-18). The polymer network model can be arranged in series or parallels to describe the large strain deformation and strain rate dependence of polymer deformation. The three-network polymer model was used in this study as it sufficiently describes a semicrystalline polyamide 6,6 under large plastic deformation (Ref 8).

Cold spray deposition still faces difficulties in coating metals on polymer substrates. Typically, a single particle can impinge on the polymer substrate and either embed or recoil from the substrate. Continuous particle coating on a polymer substrate remains challenging and recoil. Generally not only wastes the powders but destroys the already coated surface. Prior studies have addressed a qualitative process window for spraying (Ref 2, 19). Still, the lack of understanding between the coating process's connection and the material structure (as-sprayed substrate) remains. Many simulations to predict process parameters consider metal (particles) impacting metal (substrates) (Ref 19-22). These simulation results demonstrated that particle/substrate morphology changed with increase in velocity and addressed the kinetic energy to initiate the bonding between the interface. However, quantitative simulation for metal/ceramic to polymer coating remains relatively unexplored.

To address the above issue, the current study uses a polymer model implemented in an FEA code to capture the response of metal and ceramic particles impacting a polyamide substrate, and to define conditions where the particle (both those which may deform, Cu, and those unlikely to plastically deform, here chosen as ceramics for a stiff model particle) will embed and provide a basis for subsequent will adhered coatings. The polymer model used was based on experimental high strain-rate impact results. A range of parameters such as particle velocity, particle size, and the material property was studied to understand the influence of mechanical attachment of the particle onto the polymer substrate. The FEA's numerical results were compared and validated with experimental results

measurements of embedded/adhered metal and ceramic particles.

Experimental Procedure

Material Selection and Process

Two types of commercial powders were used in this study: aluminum oxide (Al_2O_3) and Cu. Both suppliers specified a minimum purity of 99.99%. The average particle size was measured by a Malvern Morphologi G3-ID particle shape analyzer (Malvern Instruments Ltd, UK), and the results are listed in Table 1. Figure 1 shows the spherical morphology of Al_2O_3 and Cu taken from the scanning electronic microscopy (SEM, JEOL-6500F) and does show the presence of some satellite particles on the alumina, which charge during imaging conditions.

The substrate chosen for this study was a polyamide 6,6 sheet with a thickness of 3.175 mm (ePlastic Co., USA). The polyamide 6,6 was cut into strip coupons according to the ASTM D638-14 (Ref 23). Cold spray deposition was carried out using a low-pressure Cold Spray K205/407R model made by Rus Sonic Technology, Inc. The air pressure was connected through the converging-diverging (CD) nozzle. The input pressure into the cold spray nozzle was adjusted following the target particle velocity. The distance between the spray nozzle to the polymer substrate is set as 30 mm, gun traverse speed 10 mm/sec. The spray gun was fixed to the z-axis while allowing the nozzle to move freely only on the x and y-axis. The microstructure of the as-sprayed specimens was investigated using the scanning electronic microscopy (SEM, JEOL-6500F).

Two-Disk (Plate)rotary System

In defining the process window for creating a well-adhered coating on a polymer substrate in the case where the particles embedded in the substrate, the particle velocity is a crucial model input, and so rather than assume linearity with applied gas pressure, this research chose to measure the particle velocity with a simple device. Figure 2 shows the setup of the two-disk rotary system for particle velocity measurement. The two-disk rotating system consists of a shaft with two plates of a fixed separation distance on the metal rod, based on prior instruments used to measure shot velocity in peening operations (Ref 24) research. To capture the particle velocity expected for cold spray (which is higher than in shot peening processes), a minimum speed of 10000 RPM was used to capture the particle impact velocity. An example of the cold spray Cu particle onto the second plate is shown in Fig. 3.

Table 1 Feedstock powders properties

Powders	Morphology	Supplier	Density, g/cm ³	Particle size range, μm (Vendor)	D ₅₀ , μm (Measured)
Al ₂ O ₃	Spherical	Inframat Advanced Materials Inc.	3.95	5–45	10
Cu	Spherical	Chemical Store Inc.	8.96	5–44	36

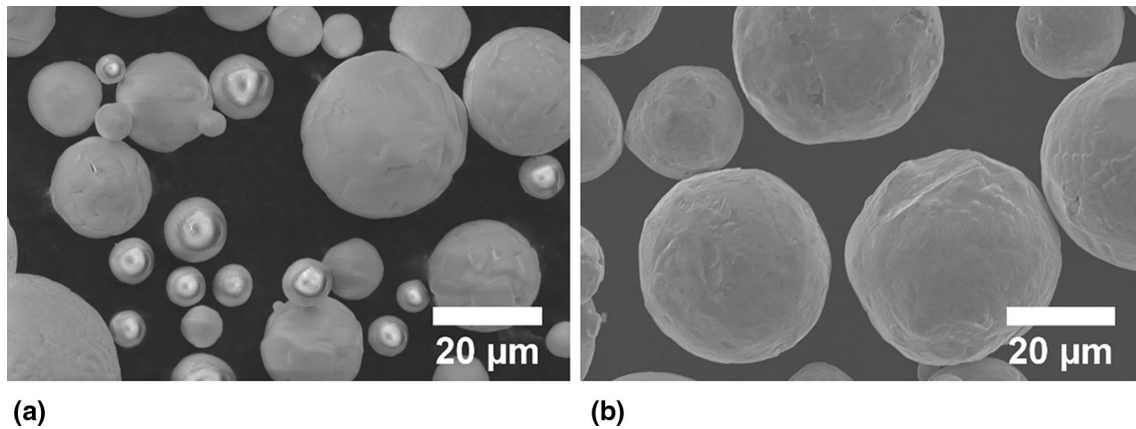
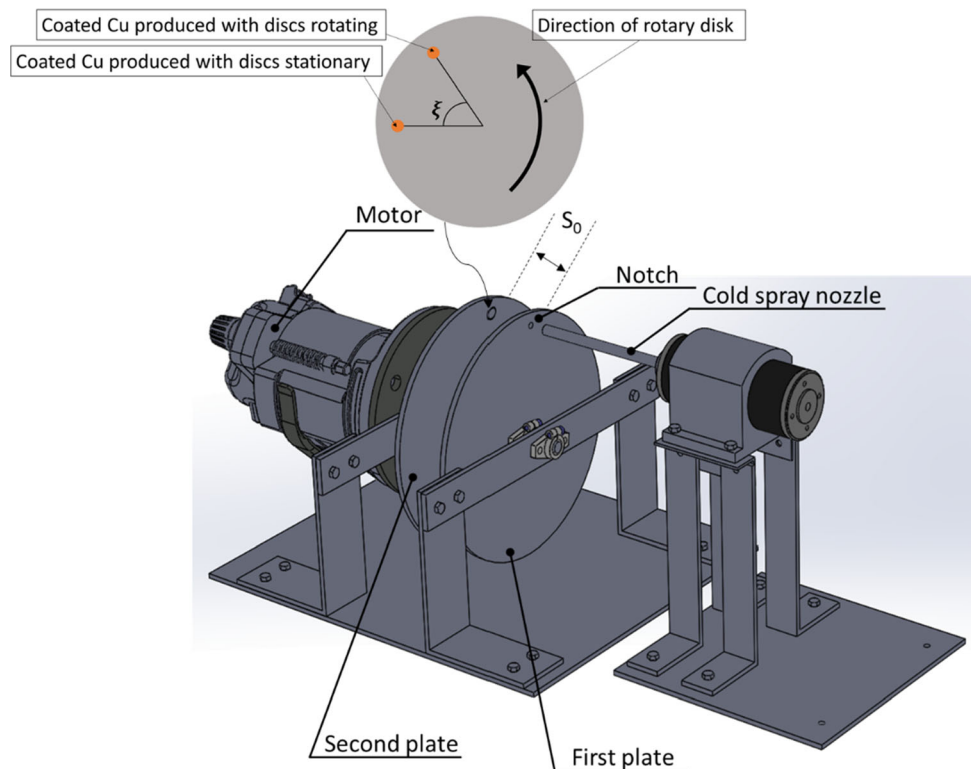


Fig. 1 SEM images of (a) Al₂O₃, (b) Cu

Fig. 2 The setup of the two disk rotary system



This cold spray system’s input air pressure (i.e., pre-nozzle) was between 0.4 and 0.65 MPa. The two plates rotate at 10,000 RPM, and a tachometer was used (Extech RPM 33) to measure the rotational speed. The distance

between the cold spray nozzle to the second plate is 33 mm. While the two-disk plate system was rotating, the particles were sprayed through a notch on the first plate, leading to deposition onto the second plate. The angle

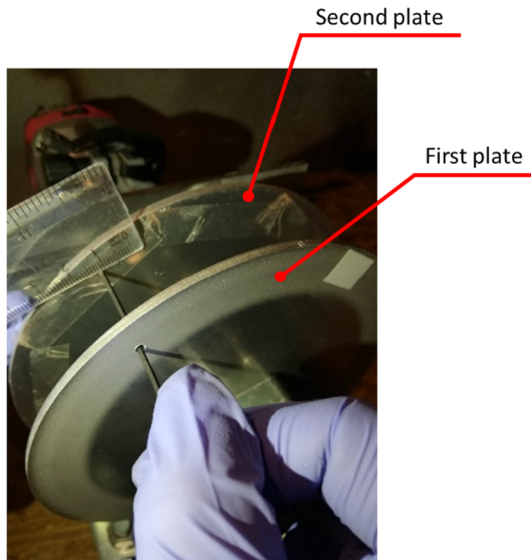


Fig. 3 The experiment result shows the coating marked on the second plate

differences were to be measured compared to the first and the second plate. The particle impact velocity, V , is

$$V = \frac{\pi \cdot n \cdot S_0}{\xi} \tag{Eq 1}$$

where n is the rotational velocity of the disk (rad/min), S_0 path of a particle between the first and the second plate, and ξ the angle differences from the initial position

Cu particles were used to quantify the input pressure correlation with particle impact velocity, as shown in Fig. 4. Five different input pressures values within 0.4 to 0.65 MPa were tested for particle velocity. Each set was done five times, and the standard deviation was plotted along with the average. In the experiment, a range of particles is cold sprayed through the plate. It is noteworthy to mention that the average particle impact velocity likely depends on many factors such as particle size, nozzle stand-off distance, driving gas condition, and is nonlinear in our current system, demonstrating the need to measure velocity if that is to be one of the parameters in the model. The observed 10% standard deviation is typical for this type of measurement compared to other published research results (Ref 24, 25).

Numerical Method

Material Model

Cold spray deposition of Cu particles on polyamide 6,6 substrate was simulated using a three-network polymer model from references (Ref 7, 15-18); this model consists

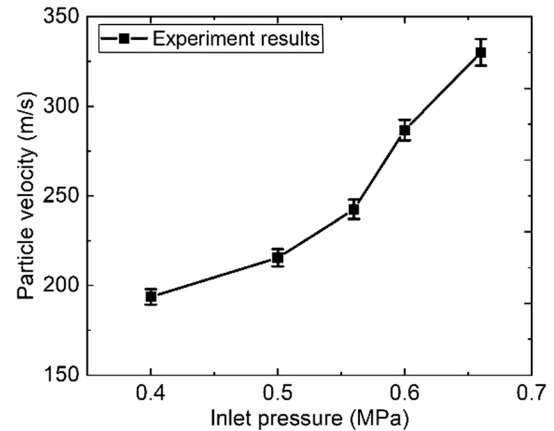


Fig. 4 The measured output of particle velocity as a function of input air pressure for this cold spray system

of three parts (molecular networks) connected in parallel (Ref 26). A schematic representation of the model is shown in Fig. 5. The three networks are stated as A , B , and C . The first two parallel networks A and B described the semicrystalline’s initial deformation and the amorphous domains. It is assumed that the temperature is constant at room temperature 273 K. In contrast, network C represents a substantial strain response after the initial response from the first two parallel networks A and B . The rigorous calibration and the validation of the three-network polymer model have already been done by others (Ref 7, 8, 15-18, 27). The available results produce from the high strain rate of polyamide 6,6 to calibrate the three-network polymer model for the cold-sprayed polymer substrate. The following constitutive equation is shown in:

$$\sigma_A = \frac{\mu_A}{J_A \bar{\lambda}_A^{e^*}} * \frac{\mathcal{L}^{-1}\left(\frac{\bar{\lambda}_A^*}{\lambda_L}\right)}{\mathcal{L}^{-1}\left(\frac{1}{\lambda_L}\right)} * \text{dev}[b_A^{e^*}] + \kappa(J_A^e - 1)I \tag{Eq 2}$$

$$\sigma_B = \frac{\mu_B}{J_B \bar{\lambda}_B^{e^*}} * \frac{\mathcal{L}^{-1}\left(\frac{\bar{\lambda}_B^*}{\lambda_L}\right)}{\mathcal{L}^{-1}\left(\frac{1}{\lambda_L}\right)} * \text{dev}[b_B^{e^*}] + \kappa(J_B^e - 1)I \tag{Eq 3}$$

$$\sigma_C = \frac{\mu_C}{J \lambda_{\text{chain}}} * \frac{\mathcal{L}^{-1}\left(\frac{\lambda_{\text{chain}}}{\lambda_L}\right)}{\mathcal{L}^{-1}\left(\frac{1}{\lambda_L}\right)} * \text{dev}[b^{e^*}] + \kappa(J - 1)I \tag{Eq 4}$$

where $J_A^e = \det[F_A^e], b_A^{e^*} = J_A^{e-2/3} F_A^e (F_A^e)^T, \bar{\lambda}_A^{e^*} = \left(\text{tr}[b_A^{e^*}/3]\right)^{1/2}, \mathcal{L}(x) = \coth(x) - \frac{1}{x}$, μ_A and μ_C are the shear modulus of network A and network C , λ_L is the locking stretch, μ_{Bi} and μ_{Bf} are the initial and final shear modulus of network B , and κ is the bulk modulus.

As shown in Fig. 5(a), the total effects of the Cauchy stress in the polymer system are given by the sum of the

Fig. 5 (a) Schematic of the constitutive models for polyamide, (b) stress vs. strain, (c) stress vs. time, (d) stress vs. strain at a strain rate range from -10^0 to -10^7

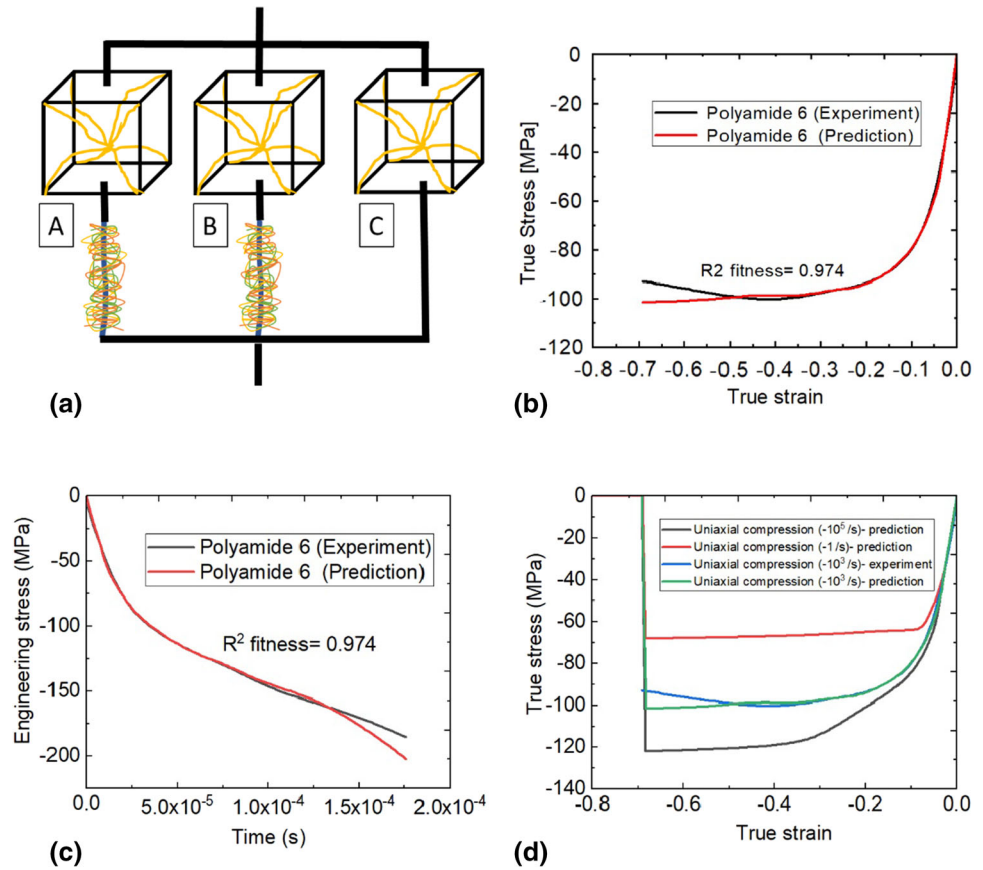


Table 2 Material constants used in the three-network model (polyamide substrate)

Material property	Material constants
μ_A (MPa)	94.124
λ_L	3.59
Kappa (MPa)	5000
μ_{Bi} (MPa)	367.67
μ_{Bf} (MPa)	116.68
β	9.16
μ_c	5.53×10^{-5}

stresses in the three-network polymer model. The material constants were formulated from the experimental results of a Split-Hopkinson pressure bar test applied to the polymer substrate. The material constants were optimized, and the material constants showed an R^2 fitting of 0.974 compared with the experimental results plotted in Fig. 5(b). The material constants used in the current study are given in Table 2. Engineering stress with time is plotted in Fig. 5(c). The input of the experiment results has a strain rate of 3000 s^{-1} . A range of polymer strain rate $1000\text{--}3000\text{ s}^{-1}$ was used

as an input to make sure the material constants agree well with the experimental results. While still having a good fitting with the experiment results, the material constants might vary. Although specific input ranges are adjusted for each material constant, the various output would still show a potentially good fit with the experimental results. Multiple trials were conducted to narrow down the parameter ranges. In this study, Drucker stability was tested to evaluate the consistency of the material constant for the three-network polymer model. The material constants with the highest uniaxial compression strain range were chosen, ranging from 0 to -0.7 . The true strain versus true stress was plotted for various strain rates from 1 s^{-1} to 10^5 s^{-1} in Fig. 5(d).

The simulation of a single Cu particle impacting the metal substrate has been widely studied (Ref 21, 28). Results show that the Preston–Tonks–Wallace (PTK) model does well results capturing the metal deformation geometry after cold spray impact (Ref 29, 30). Other alternatives, such as modifying the Johnson–Cook (J–K) model at a specific range of strain rate, accommodate the stress softening during high-speed impact (Ref 31–33).

The J–K plasticity model has been assigned to describe the Cu particle’s deformation when it impacts the polymer substrate. The metal particle plastic deformation is not the

Table 3 Cu material constants used in the Johnson–Cook plasticity model

Material property	Material constants
ρ (kg/m ³)	8.9×10^3
G (GPa)	44.7
A (MPa)	90
B (MPa)	292
n	0.31
C (MPa)	0.025
m	1.09
T_m (K)	1356
T_o (K)	298

focus in this study because of the particle impinging into a soft material; less to no plastic deformation should occur on the metal particles. Thus, using the J–K plasticity model should be sufficient. The material constants for the material model are listed in Table 3. The Cu material deformation used the J–K plasticity model that considers the strain hardening, strain rate hardening, and thermal softening. The formula is described as:

$$\sigma = [A + B\varepsilon^n][1 + C \ln \dot{\varepsilon}^*][1 - T^{*m}] \quad (\text{Eq 5})$$

where A is yield stress, B is hardening constant, C is strain rate constant, n is hardening exponent, m is thermal softening exponent, and T is temperature variation

A calibrated Drucker–Prager plasticity model, with the equation of state and Johnson–Cook rate dependence, was used to describe the Al₂O₃ impacting on the polymer substrate in the FEA simulation (which expected to show little if any plastic deformation). The material constants were taken from the Johnson–Holmquist (JH-2) ceramic material models and rearranged the Drucker–Prager plasticity model's equations to describe the Al₂O₃ particle impacting on the polymer substrate (Ref 34–37). The Drucker–Prager exponent yield criterion is provided as (6):

$$F = aq^b - p - p_t \quad (\text{Eq 6})$$

and (7):

$$p_t = a\sigma_C^b - \frac{\sigma_C}{3} \quad (\text{Eq 7})$$

where a and b are material parameters, p_t is the hardening parameter, and σ_C is uniaxial compression stress

Rearranging equation (6) shows Eq 8:

$$q = \frac{1}{a^{\frac{1}{b}}}(P + P_t)^{\frac{1}{b}} \quad (\text{Eq 8})$$

Table 4 Al₂O₃ material constants used in the Drucker–Prager plasticity model

Material property	Material constants
ρ (kg/m ³)	3.95×10^3
G (GPa)	91
P_t (GPa)	0.2
a	0.0029799
B	1.67
σ_C (GPa)	1.76
C	0.0091
C_0	576,000
S	0.5

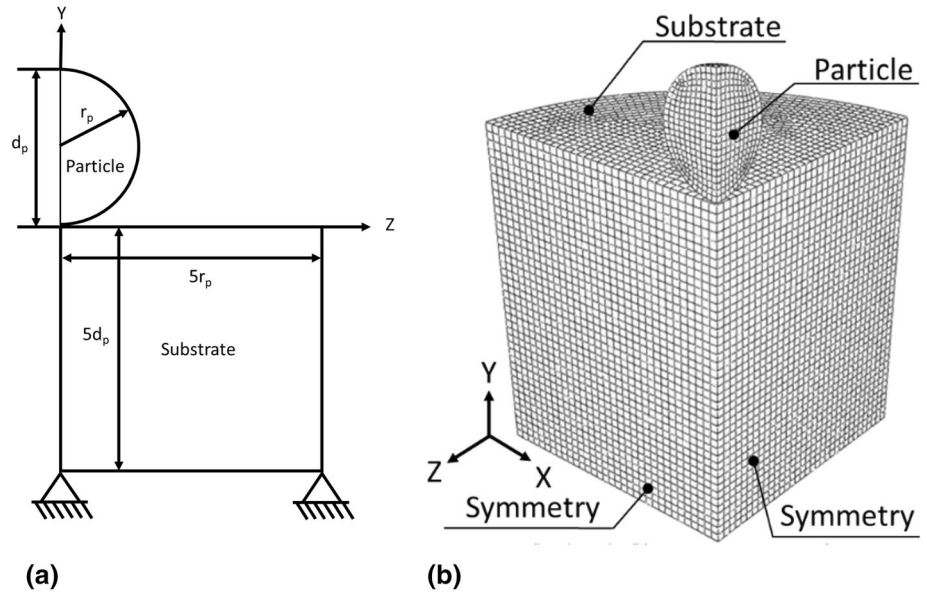
Equation 8 has a similar expression compared with the JH-2 model, and therefore comparing the equation of the JH-2 model, the engineering constants are calculated in Table 4.

Simulation Properties

A single Cu and Al₂O₃ particle impacting a polyamide substrate was simulated using FEA software (ABAQUS/Explicit 2018) with the Lagrangian approach. A ¼ of the symmetric model was conducted due to the nature of the axisymmetric geometry. Figure 6(a) and (b) shows designed geometry and boundary conditions. It was assumed that a perfectly spherical shape particle impacts on the substrate in the vertical direction. The geometry was partitioned to accommodate the mesh element and mesh density. The bottom substrate is encastre, while the surfaces on both sides are symmetrical. The symmetric boundary conditions were applied to both the X-plane and the Z-plane of the substrate geometry. The particle undergoes an adiabatic process, and both the particle and the substrate are selected as C3D8R (average strain an 8-node linear brick with reduced integration).

The particle and the substrate interaction used the available general contact, which is a node-to-surface method. When the failure criteria are met, the elements are deleted. This ensures the particle continues impacting into the polymer substrate with the interior element eroded smoothly. The hard contact model was used for the pressure–overclosure relationship. A finite sliding formulation was also used to allow the particle to move between the substrate during the impact. The interaction between the particle and the substrate uses the Coulomb friction model for modeling the friction. The friction coefficient is set as 0.002. This assumes that the particle travels at a high impact velocity that friction plays less of a role in adhering onto a polymer substrate. The research between the particle

Fig. 6 (a) Initial conditions used for the impact of the metal particle on the substrate, (b) mesh geometry and the schematic view of the FE model



and the substrate ratios limits the geometry size while maintaining a practical computation calculation. Most articles have pointed out that the particle impact onto the substrate causes the stress to propagate and reflect onto the particle because of the boundary condition set on the substrate (Ref 32, 33). A parametric study effect of the particle and the substrate ratios, mesh size, and hourglass control have been done. This parametric study showed the particle/substrate ratio can be set as 1:5 without influencing the stress wave reflection. Furthermore, the mesh size and hourglass control effect were examined to compare mesh dependency while using the hourglass control to mitigate mesh distortion. The results showed that with mesh size set for the particle as $0.15 d_p$ and the substrate as $0.1 d_p$ required less computation time while the particle's rebound velocity remains consistent with increase in mesh size. (The d_p stands for particle diameter). While the particle is traveling at a high impact velocity, it is assumed that the material reaches a specific strain range and fracture at the polymer substrate's contact region. In this research, it was assumed that the polymer substrate fails as the strain reaches 1.4.

Results and Discussion

Figure 7(a) shows an example of the polymer substrate interlocking the embedded Cu particle ($30 \mu\text{m}$) with the particle impact velocity at 300 m/s . The particle generally retains its original shape while penetrating the polymer substrate. Figure 7(b) shows the total energy distribution diagram. The total energy is the total amount of friction dissipation energy, internal energy, and kinetic energy. The

total energy is constant with increase in time. In addition, the internal energy is the total amount of plastic dissipation energy, strain energy, and artificial energy. Each of the energy quantities shows the total equivalent amount adding toward the internal energy with increase in time. The plastic dissipation energy rises significantly with the decrease in the kinetic energy. The strain energy increases as the particle impacts the polymer substrate. As the particle kinetic energy reaches the lowest value, the strain energy and the internal energy are highest. After, the strain energy starts to decrease as the portion of the energy is transferred to the kinetic energy and the plastic dissipation energy, allowing the particle to rebound.

Eventually, the kinetic energy goes to zero, and the particle is interlocked in the polymer substrate. Figure 7(c) shows the substrate strain's evolution, and the particle velocity increases with time. The strain energy recovers 43%, resulting in the strain energy to transfer parts of its energy onto the particle and causing the particle to rebound. Four different times were extrapolated and sub-plotted in Fig. 7(c) to show each FEA results. In case (1), the particle penetrates the polymer substrate. In case (2), the particle begins to rebound with the polymer substrate recovery. For case (3) and case (4), the particle separates from the polymer substrate's bottom but remains attached to the polymer substrate.

Figure 8(a) shows the Al_2O_3 particle ($30 \mu\text{m}$) rebound after impacting the polymer substrate at 300 m/s . The plastic strain is shown in the polymer substrate, while no plastic deformation occurs on the Al_2O_3 particle. Figure 8(b) shows the total energy distribution diagram. The total energy is constant with increase in time, and each portion of energy adds up to the total sum of the total

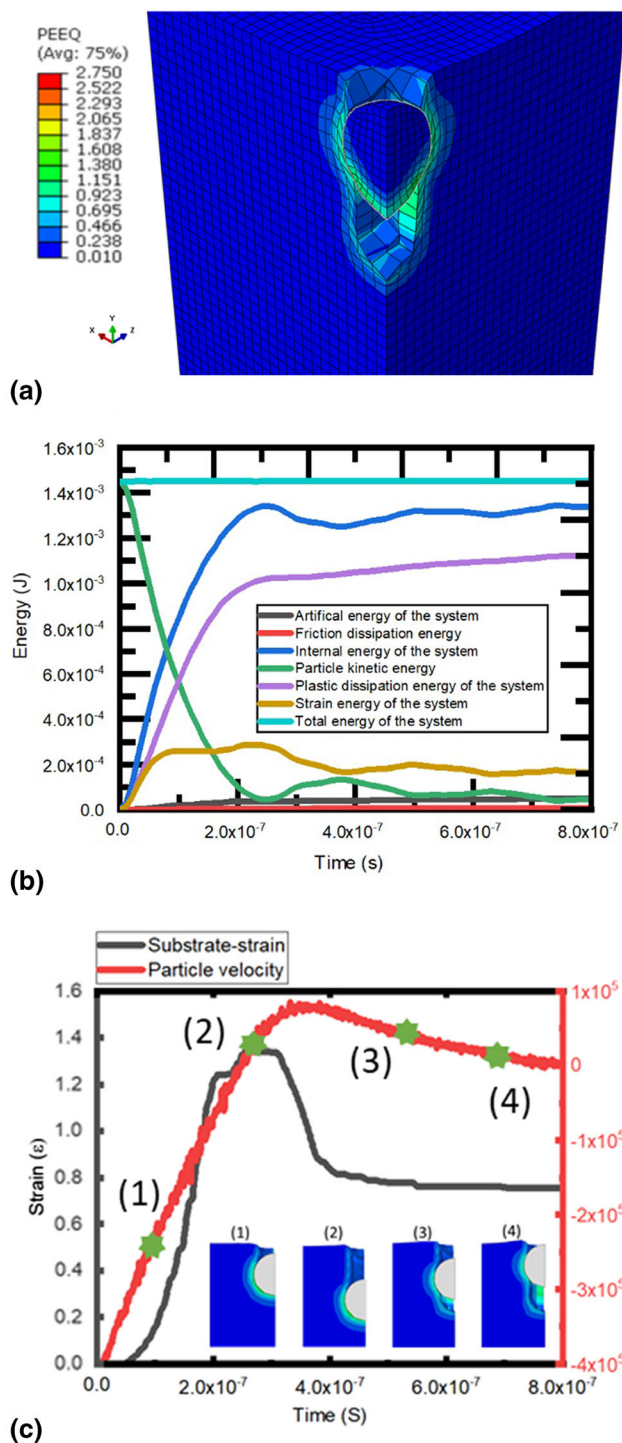


Fig. 7 (a) Plastic strain distribution of the particle (Cu) and the substrate (polyamide), (b) evolution of energy distribution, (c) strain and particle velocity in 30 μm particle and the substrate during the entire process at an impact velocity of 400 m/s

energy. The result shows that the Al_2O_3 particle retains 19.5% kinetic energy after impacting the polymer substrate. The Al_2O_3 particle retains a large portion of kinetic energy with increase in time and allows the particle to

rebound. This shows with the same particle size and impact velocity; Al_2O_3 particles are likely to rebound compared to Cu particles.

The rebound velocity for all cases between particle velocity from 100 to 500 m/s and particle size from 10 to 50 μm was conducted. The rebound velocity results were then plotted as the kinetic energy lost (η) show in (9). The formula for a fraction of kinetic energy lost (η) (9):

$$\eta = \frac{V_{\text{in}}^2 - V_{\text{r}}^2}{V_{\text{in}}^2} \quad (\text{Eq 9})$$

where V_{in} is the particle impact velocity and V_{r} is the particle rebound velocity.

When the η is close to 1, the particle is sticking, and closer to 0, it departs from the substrate. The rebound velocity is considered in this research to identify the particle interlocking in the polymer substrate (particle sticking in the substrate). The lower the rebound velocity, the particle is more inclined to adhere to the substrate. This concept assumes that a high-speed particle penetrates the substrate. However, in terms of plotting as the rebound velocity or kinetic energy, the η value was chosen to be plotted. This is because η value gives more precise, normalized, distinct results, indicating that the particle is more prone to stick onto the polymer substrate with increase in particle size and impact velocity.

Figure 9(a) and (b) shows the η with increase in particle size and particle velocity of the Al_2O_3 and Cu. The plotted diagram shows the particle size in the field of 10–50 μm for reflecting with the commercial particles distributed range in Fig. 1. The η value in the mapped diagram shows that Cu with the same particle size compared with the Al_2O_3 has a better chance of coating on the polymer substrate under the same particle velocity. Al_2O_3 particles need a particle velocity of higher than 400 m/s to have a η higher than 0.9 for the particle to coated on the polymer substrate. As to Cu, particle velocity reaching a 300 m/s already has η value higher than 0.9. The total kinetic energy of the particle dictates the overall polymer substrate deformation. At constant particle velocity, the increased particle size increased the kinetic energy and vice versa. With increase in particle size and particle velocity, particles are inclined to adhere to the polymer substrate. However, with the mapped η value, a quantitative region can be predicted—the mapped diagram provided information for narrowing down the coating parameters' prospect. The simulation results provide the future users a minimum effort for coating on a polymer substrate without wasting time and material. Thus, the objective is to understand the particle's minimum η value to attach to the polymer substrate. Vertical lines were drawn upon Fig. 10(a) and (b) at particle velocity 200 and 300 m/s (Al_2O_3 and Cu). Figure 10(a) shows that Al_2O_3 at

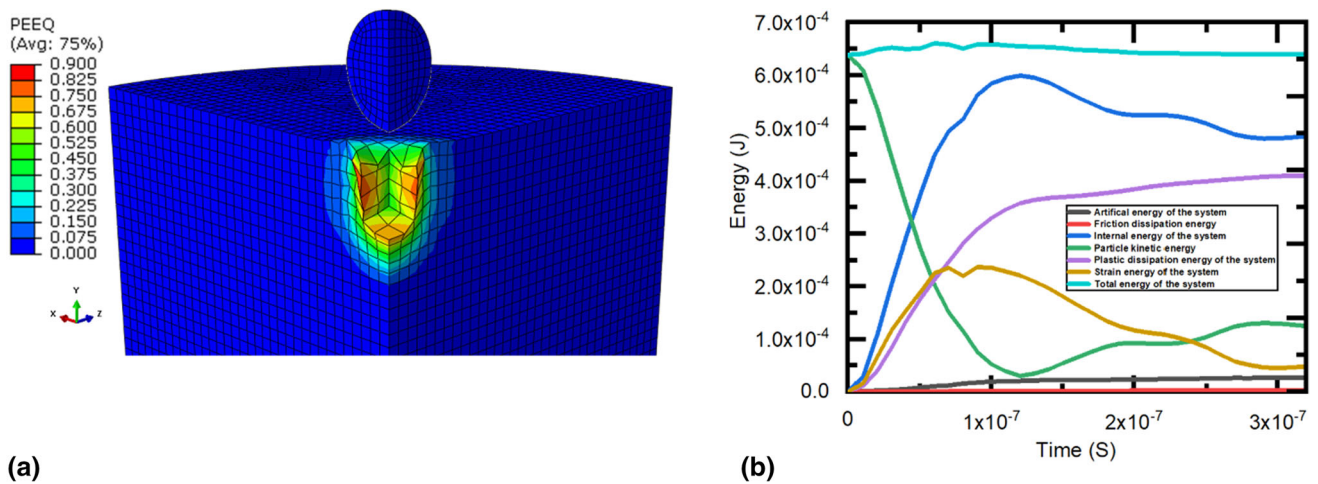


Fig. 8 (a) Plastic distribution for the particle (Al_2O_3) and the substrate (Polyamide), (b) evolution of energy distribution

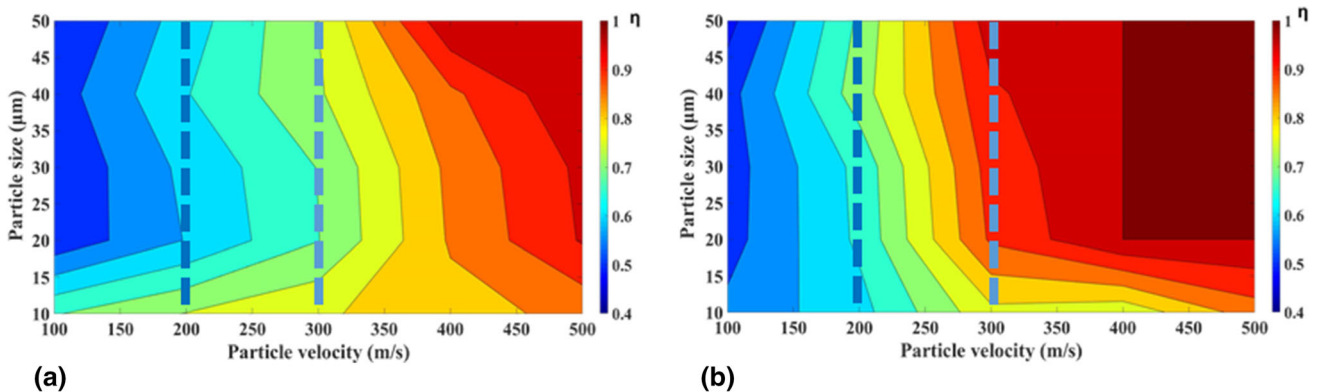


Fig. 9 Effect of particle size vs. particle velocity (a) Al_2O_3 , (b) Cu

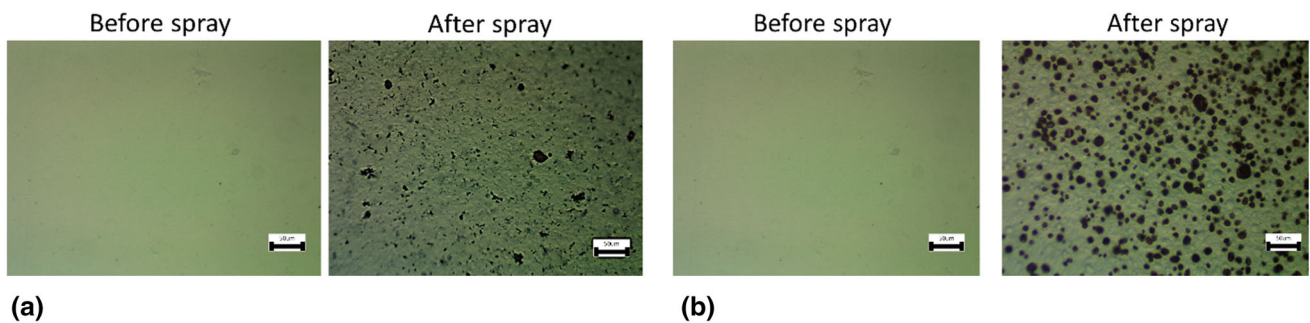


Fig. 10 Experimental results show the sprayed powders at 300 m/s with (a) Al_2O_3 before and after, (b) Cu before and after on the polyamide substrate (scale bar is 50 μm in all figures)

200 and 300 m/s has a η value smaller than 0.8, resulting in no coating. In Fig. 10(b), the η value shows that Cu particles at an impact velocity of 300 m/s with particle size range higher than 20 μm ($\eta > 0.9$) were able to be successfully coated onto the polymer surface. In contrast, Cu at 200 m/s was not successfully ($\eta < 0.75$).

Al_2O_3 and Cu particles at 300 and 200 m/s were cold sprayed onto the polymer substrate, as shown in Fig. 10(a)

and (b) and 11(a) and (b). The particle velocity was controlled by the input pressure with the results provided in Fig. 4. In Fig. 10(a) and (b), the experiment results show that only Cu particles attach to the polymer substrate at 300 m/s. The Cu particles coverage on the polymer substrate was 31 %. Simultaneously, Al_2O_3 rebounded from the polymer surface with particle velocity at 300 m/s (a few Al_2O_3 residual particles were present but not as significant

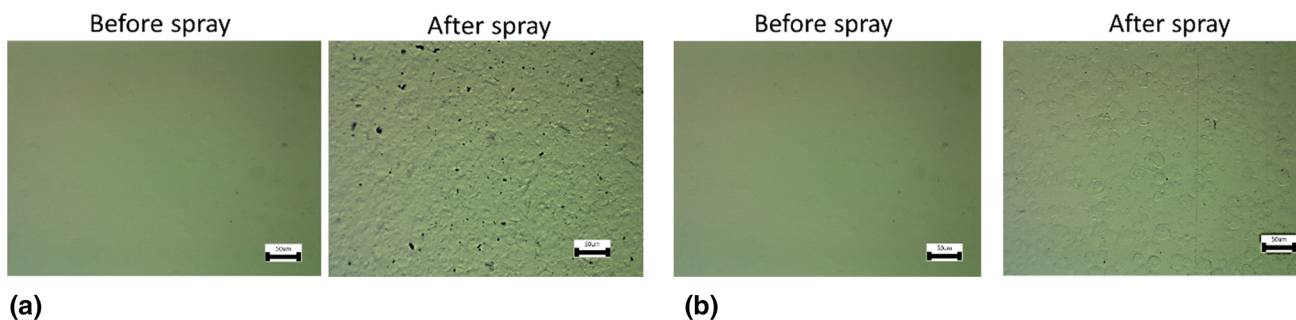


Fig. 11 Experimental results show the sprayed powders at 200 m/s (a) Al_2O_3 before and after, (b) Cu before and after on the polyamide substrate (scale bar is 50 μm in all figures)

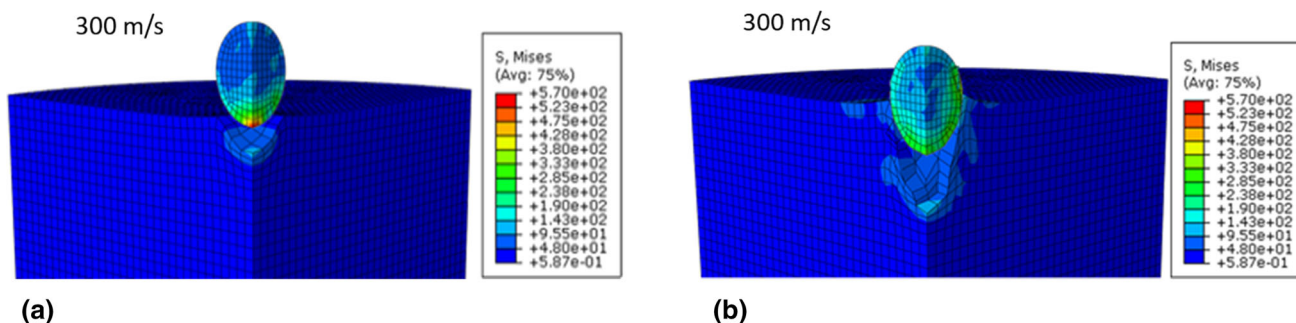


Fig. 12 Simulation results show the particle at 300 m/s (a) Al_2O_3 , (b) Cu

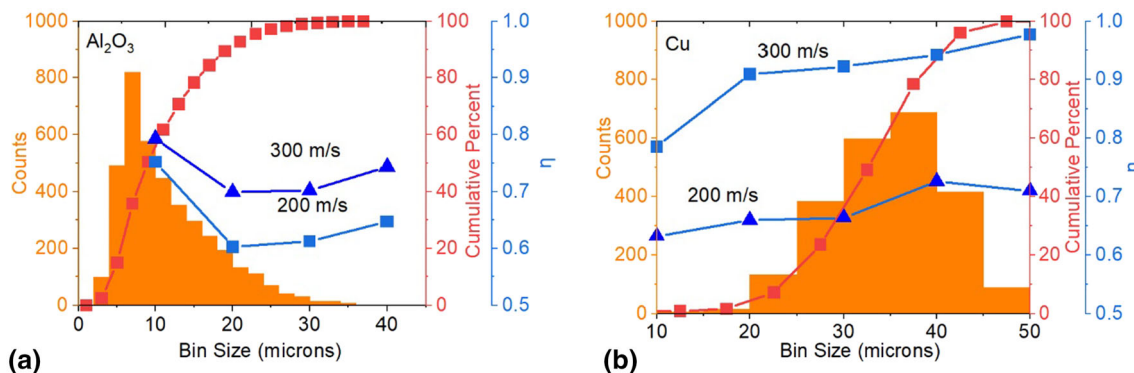


Fig. 13 Particle at 300 m/s and 200 m/s with the response of the η , particle counts, and the cumulative particle distribution for (a) Al_2O_3 , (b) Cu after impacting polyamide substrate

as Cu particles attaching onto the polymer substrate). No large coating of particles is attached to the polymer surface with the particle velocity at 200 m/s, shown in Fig. 12(a) and (b). The surface of the polyamide shows the traces of the particle rebound after cold spray. Thus, the simulation results in Fig. 9 show that Al_2O_3 and Cu agree well with the experiment results in Fig. 11(a) and (b). The experiment results also show that the particle size embedded in the polymer substrate is generally bigger than 10 μm . The simulation results of an Al_2O_3 and Cu of 30 μm size impacting the polymer substrate at 300 m/s are shown in Fig. 12(a) and (b). Results show that Cu remains in the

polymer substrate, while Al_2O_3 already rebounds from the polymer substrate at the same amount of time. Figure 13(a) and (b) shows the Al_2O_3 and Cu particle impact velocities at 300 and 200 m/s of the cumulative particle size distribution and the η with increase in particle size. The η value from Fig. 9(a) and (b) is superimposed in Fig. 13(a) and (b). Results indicate that particle size increases and results in a decrease in η value. Figure 13(a) shows Al_2O_3 particles distribution low η at 300 m/s and 200 m/s. Figure 13(b) shows that Cu particles have a high η relative 300 m/s over 200 m/s. As Fig. 11(b) shows, the Cu has a coverage of the polymer surface of 31%. Thus, it is assumed in Fig. 13(b)

that particle size accumulation is about 69 %. The η value is about 0.92, where η value closer to 1 guarantees a high coverage of the polymer material substrate.

Conclusion

A three-network polymer model was used in this study to capture the plastic deformation of the substrate from the high-speed impact caused by cold-sprayed Cu and Al₂O₃. This model was calibrated with the already available polymer high-strain rates experiment results. The cold spraying process parameters entail a specific microstructure that influences the sprayed polymer substrate's mechanical properties. A two-disk (plate) rotary system was developed to easily measure the particle velocity, a needed parameter for the model. The results show that an increase in particle kinetic energy results in an increase in the polymer viscoplastic deformation. As a result, the particles are less likely to rebound due to the decrease in strain energy and the gain of plastic deformation energy. The fraction of kinetic energy lost, η , above 0.9, shows good correspondence to the experimentally observed adhesion of the particles and allows for the prediction of process windows for a variety of materials. The numerical results have been mapped into diagrams from the responses of the particle's kinetic energy lost after impacting and further validate the experiment results of cold spraying Al₂O₃ and Cu powders on the polyamide substrate. This study demonstrates a model that provides a way to minimize the trial and error processes for identifying successful cold spray deposition on polymer substrates.

References

1. P. Cavaliere, *Cold-Spray Coatings—Recent Trends and Future Perspectives*, Springer, 2018.
2. R. Gonzalez, H. Ashrafzadeh, A. Lopera, P. Mertiny and A. McDonald, A Review of Thermal Spray Metallization of Polymer-Based Structures, *J. Therm. Spray Technol.*, 2016, **25**(5), p 897–919.
3. P.C. King, A.J. Poole, S. Horne, R. de Nys, S. Gulizia and M.Z. Jahedi, Embedment of Copper Particles into Polymers by Cold Spray, *Surf. Coat. Technol.*, 2013, **216**, p 60–67.
4. C. Chen, X. Xie, Y. Xie, X. Yan, C. Huang, S. Deng, Z. Ren and H. Liao, Metallization of Polyether Ether Ketone (PEEK) by Copper Coating via Cold Spray, *Surf. Coat. Technol.*, 2018, **342**, p 209–219.
5. C. Buckley, P. Dooling, J. Harding and C. Ruiz, Deformation of Thermosetting Resins at Impact Rates of Strain. Part 2: Constitutive Model with Rejuvenation, *J. Mech. Phys. Solids*, 2004, **52**, p 2355–2377.
6. C.R. Siviour, S.M. Walley, W.G. Proud and J.E. Field, The High Strain Rate Compressive Behaviour of Polycarbonate and Polyvinylidene Difluoride, *Polymer*, 2005, **46**(26), p 12546–12555.
7. A.D. Mulliken and M.C. Boyce, Mechanics of the Rate-Dependent Elastic–Plastic Deformation of Glassy Polymers from Low to High Strain Rates, *Int. J. Solids Struct.*, 2006, **43**(5), p 1331–1356.
8. S. Sarva, A.D. Mulliken and M.C. Boyce, Mechanics of Taylor Impact Testing of Polycarbonate, *Int. J. Solids Struct.*, 2007, **44**(7), p 2381–2400.
9. H.-S. Shin, S.-T. Park, S.-J. Kim, J.-H. Choi and J.-T. Kim, Deformation Behavior of Polymeric Materials by Taylor Impact, *Int. J. Mod. Phys. B*, 2008, **22**(09n11), p 1235–1242.
10. D.R. Drodge, B. Mortimer, C. Holland and C.R. Siviour, Ballistic Impact to Access the High-Rate Behaviour of Individual Silk Fibres, *J. Mech. Phys. Solids*, 2012, **60**(10), p 1710–1721.
11. M.I. Okereke, C.P. Buckley and C.R. Siviour, Compression of Polypropylene Across a Wide Range of Strain Rates, *Mech. Time-Dependent Mater.*, 2012, **16**(4), p 361–379.
12. P. Yu, X. Yao, Q. Han, S. Zang and Y. Gu, A Visco-Elastoplastic Constitutive Model for Large Deformation Response of Polycarbonate over a Wide Range of Strain Rates and Temperatures, *Polymer*, 2014, **55**(25), p 6577–6593.
13. M.J. Kendall and C.R. Siviour, Experimentally Simulating High-Rate Behaviour: Rate and Temperature Effects in Polycarbonate and PMMA, *Philos. Trans. A Math. Phys. Eng. Sci.*, 2014, **372**(2015), p 20130202. (in Eng)
14. J. Sweeney, A Comparison of Three Polymer Network Models in Current Use, *Comput. Theor. Polym. Sci.*, 1999, **9**(1), p 27–33.
15. J.S. Bergström and M.C. Boyce, Deformation of Elastomeric Networks: Relation Between Molecular Level Deformation and Classical Statistical Mechanics Models of Rubber Elasticity, *Macromolecules*, 2001, **34**(3), p 614–626.
16. M.C. Boyce, G.G. Weber and D.M. Parks, On the Kinematics of Finite Strain Plasticity, *J. Mech. Phys. Solids*, 1989, **37**(5), p 647–665.
17. E.M. Arruda and M.C. Boyce, A Three-Dimensional Constitutive Model for the Large Stretch Behavior of Rubber Elastic Materials, *J. Mech. Phys. Solids*, 1993, **41**(2), p 389–412.
18. E.M. Arruda and M.C. Boyce, Evolution of Plastic Anisotropy in Amorphous Polymers During Finite Straining, *Int. J. Plast.*, 1993, **9**(6), p 697–720.
19. H. Che, X. Chu, P. Vo and S. Yue, Metallization of Various Polymers by Cold Spray, *J. Therm. Spray Technol.*, 2018, **27**(1), p 169–178.
20. Z. Khalkhali, W. Xie, V.K. Champagne, J.-H. Lee and J.P. Rothstein, A Comparison of Cold Spray Technique to Single Particle Micro-ballistic Impacts for the Deposition of Polymer Particles on Polymer Substrates, *Surf. Coat. Technol.*, 2018, **351**, p 99–107.
21. S. Shah, J. Lee and J.P. Rothstein, Numerical Simulations of the High-Velocity Impact of a Single Polymer Particle During Cold-Spray Deposition, *J. Therm. Spray Technol.*, 2017, **26**(5), p 970–984.
22. A. Małachowska, M. Winnicki, Ł. Konat, T. Piwowarczyk, L. Pawłowski, A. Ambroziak and M. Stachowicz, Possibility of Spraying of Copper Coatings on Polyamide 6 with Low Pressure Cold Spray Method, *Surf. Coat. Technol.*, 2017, **318**, p 82–89.
23. “ASTM International. *D638-14 Standard Test Method for Tensile Properties of Plastics*, West Conshohocken, PA, 2014”
24. A. Fry, M. Gee, S. Clausen, U. Neuschaefer-Rube, M. Bartscher, D. Spaltmann, M. Woydt, S. Radek, F. Cernuschi, J. Nicholls, and T.W. Rose, Metrology to Enable High Temperature Erosion Testing—A New European Initiative, *Advances in Materials Technology for Fossil Power Plants—Proceedings from the 7th International Conference*, 2014, p 400–411

25. N. Haghbin, A. Khakpour, J. Schwartztruber and M. Papini, Measurement of Abrasive Particle Velocity and Size Distribution in High Pressure Abrasive Slurry and Water Micro-jets Using a Modified Dual Disc Anemometer, *J. Mater. Process. Technol.*, 2019, **263**, p 164–175.
26. J. Bergström, A. Bowden, C. Rimnac, and S. Kurtz, Development and Implementation of an Advanced User Material Model for UHMWPE, 2019
27. H. Cho, S. Bartyczak, W. Mock and M.C. Boyce, Dissipation and Resilience of Elastomeric Segmented Copolymers Under Extreme Strain Rates, *Polymer*, 2013, **54**(21), p 5952–5964.
28. J. Xie, D. Nélias, H. Walter-Le Berre, K. Ogawa and Y. Ichikawa, Simulation of the Cold Spray Particle Deposition Process, *J. Tribol.*, 2015, **137**(4), p 041101–041115.
29. S. Rahmati and B. Jodoin, Physically Based Finite Element Modeling Method to Predict Metallic Bonding in Cold Spray, *J. Therm. Spray Technol.*, 2020, **29**(4), p 611–629.
30. S. Rahmati and A. Ghaei, The Use of Particle/Substrate Material Models in Simulation of Cold-Gas Dynamic-Spray Process, *J. Therm. Spray Technol.*, 2013, **23**, p 530–540.
31. F. Qin, T. An and N. Chen, Strain Rate Effects and Rate-Dependent Constitutive Models of Lead-Based and Lead-Free Solders, *J. Appl. Mech.*, 2009, **77**(1), p 011008–1.
32. X. Wang and J. Shi, Validation of Johnson-Cook Plasticity and Damage Model Using Impact Experiment, *Int. J. Impact Eng.*, 2013, **60**, p 67–75.
33. M. Murugesan and D.W. Jung, Johnson Cook Material and Failure Model Parameters Estimation of AISI-1045 Medium Carbon Steel for Metal Forming Applications, *Materials*, 2019, **12**, p 609.
34. I.C. Sinka, J.C. Cunningham and A. Zavaliangos, The Effect of Wall Friction in the Compaction of Pharmaceutical Tablets with Curved Faces: A Validation Study of the Drucker-Prager Cap Model, *Powder Technol.*, 2003, **133**(1), p 33–43.
35. D. Cronin, K. Bui, C. Kaufmann, G.J. McIntosh, and T. Berstad, Implementation and Validation of the Johnson-Holmquist Ceramic Material Model in LS-Dyna, 2003
36. G.R. Johnson and T.J. Holmquist, An Improved Computational Constitutive Model for Brittle Materials, *AIP Conf. Proc.*, 1994, **309**(1), p 981–984.
37. T.J. Holmquist and G.R. Johnson, Characterization and Evaluation of Silicon Carbide for High-Velocity Impact, *J. Appl. Phys.*, 2005, **97**(9), p 093502.

Publisher's Note Springer Nature remains neutral with regard to jurisdictional claims in published maps and institutional affiliations.